

Analysis of an Oscillatory System With Three Coupled Coils for Wireless Power Transfer

Víctor Ardila¹, *Student Member, IEEE*, Franco Ramírez², *Senior Member, IEEE*,
and Almudena Suárez³, *Fellow, IEEE*

Abstract—In near-field power transfer, the distance between the transmitter and receiver resonators can be extended with the aid of an intermediate resonator, which may also be used to circumvent an obstacle such as a wall or desktop. Most previous works analyze the coupled system when driven by an independent source, which will typically require a power amplifier. Instead, an oscillator will be considered here, which will eliminate the need for the signal generator and driver. However, the two resonator couplings will have an impact on the oscillator behavior and its stability properties. We will initially address a cubic-nonlinearity oscillator and demonstrate that the coupled multiresonance network may lead to undesired oscillation modes. In the second stage, we will consider a transistor-based oscillator, which will be analyzed through a semianalytical formulation capable of providing all the coexisting periodic solutions. The undesired modes will be suppressed with the aid of a trap resonator. To maximize the power transfer, we will first obtain the optimum oscillator load admittance by means of a new procedure. Then, the admittance will be implemented using a relationship between the coupling factors. The methods will be applied to a Class-E oscillator, which has been experimentally characterized.

Index Terms—Bifurcation, oscillator, resonator coupling, stability, wireless power transfer.

I. INTRODUCTION

NEAR-FIELD wireless power transfer through the inductive coupling of two resonators can be applied to recharge electrical vehicles, sensor networks, and biomedical implants, among others [1], [2], [3], [4], [5], [6], [7], [8], [9], [10], [11]. However, the transferred power decreases for a larger distance between the resonators or when they get misaligned [12], [13], which is due to the reduction of the coupling factor. Previous works [14], [15], [16], [17], [18], [19], [20], [21], [22] have demonstrated the convenience of using an intermediate (or relay) resonator for applications demanding a larger distance or when an obstacle such as a wall or desktop [14], [18] must

be circumvented. Different arrangements [14], [16], [21] have been proposed, enabling power transfer at distances that are several times larger than the resonator size. Most previous research [14], [15], [16], [17], [18], [19], [20], [21], [22] focuses on analysis and optimization of a passive system of three coupled resonators driven by an independent source. However, practical applications will often require, together with an independent source, a high-power amplification stage. Alternatively, a high-power oscillator [23], [24], [25], [26], [27], [28] can be used, which eliminates the need for the signal generator and driver [25]. This should enable a higher efficiency when considering the total consumption, as shown in [23]. Although oscillator circuits have been used in systems containing a relay element [15], [22], to the best of our knowledge no in-depth investigation of oscillator behavior in these coupled conditions has been carried out. Due to the presence of the additional resonator, one may expect a more complex response than the one obtained when the oscillator is coupled to a single resonator, which has been studied in recent works in both free-running [23], [24], [25], [26], [27], [28] and injection-locked [29], [30] operation.

In this work, we will address a system composed of an oscillator coupled to an intermediate (ideally lossless) resonator, acting as a relay, and a power-receiver resonator. In these conditions, the oscillator active core will see a multiresonance load network, which may lead to undesired operation modes. For an in-depth understanding of the system behavior, we will initially carry out an analytical study of a cubic-nonlinearity oscillator coupled to the two external resonators. As shown in [19] and [20], for a sufficient distance between the transmitter and receiver inductors, their coupling effects can be neglected, so the behavior will depend on two coupling factors: between the transmitter inductor (in the oscillator) and the intermediate inductor (k_1), and between the intermediate inductor and the receiver one (k_2). We will derive the steady-state oscillation condition and obtain all the possible coexisting oscillation modes and their stability properties. Then, we will obtain the analytical relationship between the factors k_1 and k_2 that provides the load conductance required for maximum transferred power. This will facilitate an optimum selection of the distances between the inductors, as well as other relevant design parameters, such as the load resistance.

In the second stage, we will consider a transistor-based oscillator coupled to the intermediate and receiver resonators. Due to the potential complexity of the solutions, the system

Manuscript received 21 April 2023; revised 25 August 2023 and 23 October 2023; accepted 24 October 2023. This work was supported in part by the Spanish Ministry of Science and Innovation (MCIN/AEI/10.13039/501100011033) under Grant PID2020-116569RB-C31 and in part by the Consejería de Universidades, Igualdad, Cultura y Deporte del Gobierno de Cantabria (Contrato Programa Gobierno de Cantabria—UC). (*Corresponding author: Franco Ramírez.*)

The authors are with the Departamento de Ingeniería de Comunicaciones, Universidad de Cantabria, 39005 Santander, Spain (e-mail: victorangel.ardila@unican.es; ramirezf@unican.es; almudena.suarez@unican.es).

Color versions of one or more figures in this article are available at <https://doi.org/10.1109/TMTT.2023.3330366>.

Digital Object Identifier 10.1109/TMTT.2023.3330366

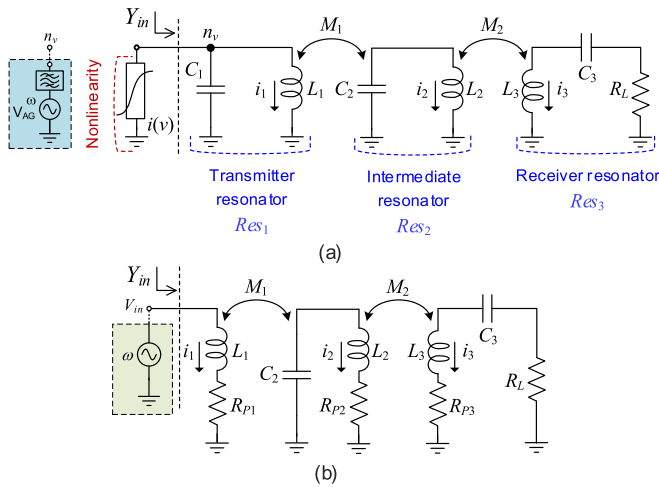


Fig. 1. Cubic-nonlinearity oscillator considered in the analytical study. It is coupled to an intermediate resonator, in turn coupled to a receiver resonator. (a) Oscillator schematic. The analytical calculations are validated with HB. The most complex oscillation curves are obtained through the optimization of a voltage AG. Element values: $i(v) = av + bv^3$ ($a = -0.01$ A/V and $b = 0.01$ A/V³), $C_1 = C_2 = 424$ pF, $L_1 = L_2 = 0.325$ μ H, $R_L = 50$ Ω , $C_3 = 70.6$ pF, and $L_3 = 1.95$ μ H. The three resonators (Res_1 – Res_3) are tuned at 13.56 MHz. (b) Calculation of the input admittance Y_{in} .

will be analyzed through a semianalytical formulation [27], [28], capable of providing all the coexisting periodic solutions. This formulation relies on a nonlinear admittance function extracted from harmonic-balance (HB) simulations, which describes the oscillator active core. All the undesired oscillation modes will be suppressed with the aid of a trap resonator. The output power will be maximized through a two-step method. In the first step, we will make use of a new oscillator output-power contour plot to obtain the optimum load admittance. In the second step, this admittance will be implemented using the relationship between k_1 and k_2 derived in the analytical study. The analysis and design methods will be applied to a Class-E oscillator that has been manufactured, and experimentally characterized.

We would like to emphasize that the novelty of this work is not the system or its implementation, but the in-depth investigation of its complex behavior. This involves the analysis of its stability properties and oscillation modes, the stabilization procedures, and the derivation of the coupling conditions that maximize the output power.

This article is organized as follows. Section II presents an analytical study of the oscillatory system with three coupled resonators, which will include the calculation of the steady-state solutions, the stability properties, and the analytical relationship between k_2 and k_1 for maximum transferred power. Section III describes the analysis of the practical Class-E power oscillator and the new two-step procedure for the maximization of the power transfer. Finally, Section IV presents the experimental characterization.

II. ANALYTICAL STUDY OF THE OSCILLATORY SYSTEM WITH THREE COUPLED COILS

For the analytical study, we will consider an oscillator circuit [Fig. 1(a)] based on the cubic nonlinearity $i(v) = av + bv^3$,

where the coefficient $a < 0$ is the small-signal conductance and the coefficient $b > 0$ will enable the saturation of the oscillation amplitude. Given that the analysis is carried out at the fundamental frequency, we will make use of the describing function [31]. This is the response of the nonlinear element to a sinusoidal input, calculated as the ratio between the fundamental component of the output and the input amplitude. Here, it is calculated as the ratio between the first harmonic of the current $i(t)$ and the amplitude of the input voltage V . This describing function is $Y_N(V) = a + \beta V^2$, where $\beta = 3b/4$. Note that for $V < (-a/\beta)^{1/2}$, the function $Y_N(V)$ will provide negative conductance because $a < 0$. The nonlinear element is loaded with a parallel resonator, composed of the inductor L_1 and the capacitor C_1 [Fig. 1(a)]. The inductor L_1 is coupled to the inductor L_2 of an intermediate resonator (acting as a relay), which is also coupled to the inductor L_3 of the receiver resonator, with a series configuration. To obtain manageable expressions, we will disregard the coupling between the transmitter and receiver resonators, which, as shown in [19] and [20], can be assumed negligible for a sufficient distance (larger than the radius of the coils). First, we will perform a stability analysis of the dc solution. Then, we will obtain the steady-state solutions (which may correspond to different oscillation modes) and analyze their stability properties. Finally, we will derive the conditions for maximum power transfer.

A. Oscillation Startup

For the oscillation startup, the dc solution must be unstable, and give rise, under any small perturbation, to an oscillatory transient, which will initially grow in an exponential manner [32], [33], [34]. To analyze the stability of the dc solution we will derive its characteristic equation [33]. This is the homogeneous equation obtained when the solution of the perturbed system is expressed as an exponential of complex frequency s [33]. As the perturbation is small, we will linearize $i(v) = av + bv^3$ about the dc solution. In the case of the circuit in Fig. 1(a), this solution is $v = 0$ and the linearization gives the (small signal) negative conductance $Y_N(V = 0) = a$. We will also evaluate the load admittance (Y_{in}), seen from the terminals of L_1 , at the perturbation frequency s . In the absence of coupling, the resulting characteristic equation is

$$Y_T(V = 0, s) = a + C_1 s - \frac{1}{L_1 s} = 0 \quad (1)$$

where $Y_T(V = 0, s)$ is the total admittance at the node n_v in small-signal conditions. For simplicity, the inductor L_1 is considered lossless. The roots of (1), also known as solution eigenvalues or poles [34], [35], determine the transient response. Solving for s one obtains

$$s = -\frac{a}{2C_1} \pm \sqrt{\frac{a^2}{4C_1^2} - \frac{1}{L_1 C_1}}. \quad (2)$$

For the oscillation startup, we must have a pair of complex-conjugate poles on the right-hand side (RHS) of the complex plane. As deduced from (2), this will require $a < 0$ and $(aL_1)^2 - 4L_1C_1 < 0$, which will give rise to the

exponential growth of the oscillation amplitude at $\omega = Im(s)$. The element values in the caption of Fig. 1 have been chosen to fulfill these conditions. Now, we will address the system in coupled operation. This will require a general calculation of the input admittance Y_{in} , seen from the coupled inductor L_1 . To obtain Y_{in} , we will connect an independent excitation voltage source V_{in} between the terminals of L_1 , as shown in Fig. 1(b), where, for the sake of completeness, the resistive losses of the three inductors (R_{pi} , where $i = 1, 2, 3$) have been considered. The resulting equation system is

$$\begin{aligned} (L_1s + R_{p1})I_1 + M_1sI_2 + 0 \times sI_3 &= V_{in} \\ M_1sI_1 + \left(\frac{1}{C_2s} + L_2s + R_{p2}\right)I_2 + M_2sI_3 &= 0 \\ M_2sI_2 + \left(R_L + R_{p3} + \frac{1}{C_3s} + L_3s\right)I_3 &= 0 \end{aligned} \quad (3)$$

where $M_1 = k_1(L_1L_2)^{1/2}$ and $M_2 = k_2(L_2L_3)^{1/2}$ are the mutual inductances between the transmitter and the intermediate inductor, and between the intermediate inductor and the receiver one. The input admittance is $Y_{in} = I_1/V_{in}$. System (3), which includes R_{pi} , will be used to evaluate the effect of the inductor losses. However, in the analytical derivations, we will neglect these losses, as done in [36] and [37], which will provide manageable expressions and better insight. Considering the continuity of the equations, we can expect a small output-power reduction, which will not affect the main conclusions of the analytical study, as will be verified.

Under $R_{pi} = 0$, Y_{in} can be expressed as the following ratio of polynomials:

$$Y_{in}(s) = \frac{(1 - k_2^2)s^4 + \omega_3 Q_3^{-1} s^3 + (\omega_3^2 + \omega_2^2)s^2 + \omega_2^2 \omega_3 Q_3^{-1} s + \omega_2^2 \omega_3^2}{L_1s \left[\begin{aligned} &(1 - k_1^2 - k_2^2)s^4 + \omega_3 Q_3^{-1} (1 - k_1^2)s^3 \\ &+ (\omega_3^2(1 - k_1^2) + \omega_2^2)s^2 + \omega_2^2 \omega_3 Q_3^{-1} s + \omega_2^2 \omega_3^2 \end{aligned} \right]} \quad (4)$$

where we have defined the following parameters:

$$\begin{aligned} Q_3^{-1} &= \omega_3 C_3 R_L \\ \omega_2^2 &= 1/(L_2 C_2) \\ \omega_3^2 &= 1/(L_3 C_3). \end{aligned} \quad (5)$$

They correspond to the quality factor of the third (receiver) resonator and the resonance frequencies of the second (intermediate) and third resonators. Note that the input admittance Y_{in} in (4) does not depend on the individual values L_2 and C_2 of the intermediate resonator but only on its resonance frequency ω_2 . In coupled conditions, we will have the following characteristic equation:

$$Y_T(V = 0, s) = a + Cs + Y_{in}(s) = 0 \quad (6)$$

which after replacement of $Y_{in}(s)$ in (4) leads to

$$\begin{aligned} (a + Cs)L_1s \left[\begin{aligned} &(1 - k_1^2 - k_2^2)s^4 + \omega_3 Q_3^{-1} (1 - k_1^2)s^3 \\ &+ (\omega_3^2(1 - k_1^2) + \omega_2^2)s^2 + \omega_2^2 \omega_3 Q_3^{-1} s + \omega_2^2 \omega_3^2 \end{aligned} \right] \\ &+ (1 - k_2^2)s^4 + \omega_3 Q_3^{-1} s^3 + (\omega_3^2 + \omega_2^2)s^2 \\ &+ \omega_2^2 \omega_3 Q_3^{-1} s + \omega_2^2 \omega_3^2 = 0. \end{aligned} \quad (7)$$

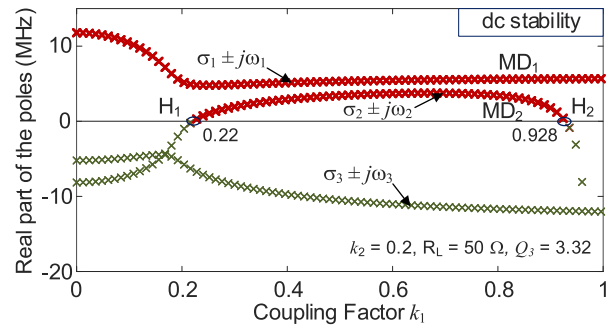


Fig. 2. Stability analysis of the dc solution of the cubic-nonlinearity oscillator in Fig. 1(a) versus k_1 for $k_2 = 0.2$. Variation of the real part of the roots of (7), providing the system poles.

The eigenvalues or poles of the dc solution ($v = 0$) are given by the roots of (7). Though some works consider the detuning of the intermediate resonator for optimization purposes [18], [19], the three resonators are typically tuned to the same frequency [14], [17]. The analysis here will be particularized to this case, so the intermediate and receiver resonators will have identical resonance frequencies $\omega_2 = \omega_3$. This common resonance frequency will agree with the free-running frequency of the oscillator in standalone (uncoupled) operation, that is, $\omega_2 = \omega_3 = \omega_0$, which in this case is $\omega_0 = 1/(L_1 C_1)^{1/2}$. The extension to other cases is possible but beyond the scope of this initial work. To illustrate the analysis, we will consider the element values in the caption of Fig. 1, which provide $f_0 = \omega_0/(2\pi) = 13.56$ MHz and $Q_3 = 3.32$. Fig. 2 presents the variation of the real part of the roots of (6) versus k_1 , for $k_2 = 0.2$. The dc solution is unstable for all the k_1 values, with at least one pair of complex-conjugate poles in the RHS, which implies the fulfillment of the oscillation startup conditions. For $k < k_{H1} = 0.22$, there is only one pair of complex-conjugate poles ($\sigma_1 \pm j\omega_1$) on the RHS. For $k_1 = 0$, this pair of poles agrees with the one in (2), corresponding to the standalone free-running oscillation. The pair of poles $\sigma_1 \pm j\omega_1$ remains on the RHS for all k_1 values (Fig. 2) and is associated with oscillation mode MD1. However, at H_1 , a second pair of complex-conjugate poles ($\sigma_2 \pm j\omega_2$) crosses to the RHS, which corresponds to a direct Hopf bifurcation [34], [38], [39]. A direct (inverse) Hopf bifurcation occurs when a pair of complex-conjugate poles crosses the imaginary axis to the RHS [left-hand side (LHS)] of the complex plane. This involves the onset (extinction) of an oscillation at the frequency of the crossing poles. As will be shown, $\sigma_2 \pm j\omega_2$ is associated with a second oscillation mode (MD2), which arises at H_1 . This second pair of complex-conjugate poles crosses back to the LHS at $k_{H2} = 0.928$ (inverse Hopf bifurcation), where MD2 is extinguished.

In a less rigorous manner, the oscillation startup conditions can be evaluated by making $s = j\omega$ and tracing the real and imaginary parts of the total admittance function $Y_T(V = 0, \omega) = a + Y_{in}(\omega)$ versus ω . The impact of k_1 and k_2 on the stability properties is shown in Fig. 3(a). In uncoupled operation, the imaginary part of the total admittance $Y_{T,i}$ crosses the horizontal axis ($\omega = 0$) only once, at $\omega_0/(2\pi) = 13.56$ MHz, with positive slope $\partial Y_{T,i}(\omega)/\partial \omega > 0$. Together

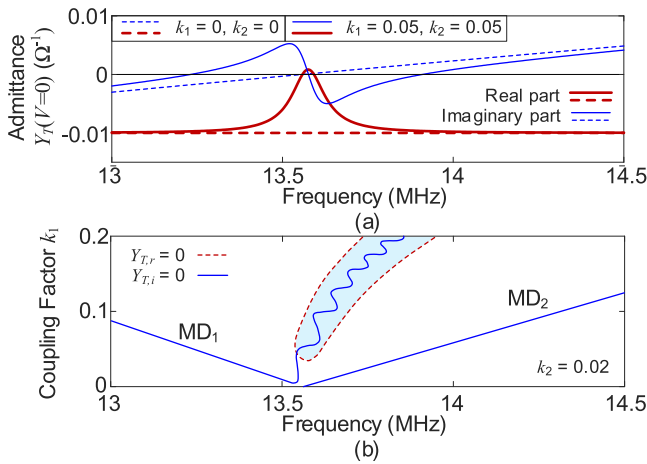


Fig. 3. Admittance analysis of the oscillation startup conditions. (a) Variation of the real and imaginary parts of $Y_T(V = 0, \omega, k_1, k_2)$ versus ω for very small values of k_1 and k_2 , equal to 0.05. The results are compared with those obtained in uncoupled conditions. (b) Contours $Y_{T,r}(V = 0, \omega, k_1) = 0$ and $Y_{T,i}(\omega, k_1) = 0$ in the plane defined by ω and k_1 when $k_2 = 0.02$.

with the negative value of the real part $Y_{T,r}(V = 0, \omega_0) < 0$, this is indicative [40] of a pair of complex-conjugate poles on the RHS and, thus, of the fulfillment of the oscillation startup conditions. Note that the analysis based on $Y_T(V = 0, \omega)$ may fail in more complex circuits due to the possible cancellations of RHS zeroes and RHS poles [41], [42]. Thus, in uncoupled conditions, the oscillation startup conditions are fulfilled at a single frequency (13.56 MHz). However, as soon as the oscillator becomes coupled, the imaginary part passes through a maximum and then a minimum, and there are two frequency values (different from the uncoupled oscillation frequency) at which the oscillation startup conditions are fulfilled.

For a more detailed analysis of the sensitivity to the coupling factors, in Fig. 3(b), we have traced the contours $Y_{T,r}(V = 0, \omega, k_1) = 0$ (dashed line) and $Y_{T,i}(\omega, k_1) = 0$ (solid line) in the plane defined by ω and k_1 when $k_2 = 0.02$. The real part $Y_{T,r}(V = 0, \omega, k_1)$ is negative everywhere in this plane except in the shadowed region, where $Y_{T,i}(\omega, k_1)$ crosses $\omega = 0$ with negative slope $\partial Y_{T,i}(\omega, k_1)/\partial \omega < 0$. In the two sections of the locus $Y_{T,i}(\omega, k_1) = 0$ indicated as MD1 and MD2, we have $\partial Y_{T,i}(\omega, k_1)/\partial \omega > 0$. Thus, for every k_1 , the oscillation startup conditions are fulfilled at two distinct frequencies, in consistency with the two detected oscillation modes (MD1 and MD2).

B. Steady-State Oscillation Conditions

For the calculation of the steady-state oscillation modes, we will represent the nonlinear element with its describing function: $Y_N(V) = a + \beta V^2$. Applying Kirchhoff's laws at node n_v , we obtain

$$Y_T(V, \omega) = a + \beta V^2 + jC\omega + Y_{in}(k_1, k_2, \omega) = 0 \quad (8)$$

where $Y_T(V, \omega)$ is the nonlinear total admittance function. It must be equal to zero to obtain $V \neq 0$. To calculate V and ω , the complex equation (8) is split into real and imaginary

parts

$$Y_{T,r}(V, \omega) = a + \beta V^2 + Y_{in,r}(k_1, k_2, \omega) = 0 \quad (a)$$

$$Y_{T,i}(\omega) = C\omega + Y_{in,i}(k_1, k_2, \omega) = 0 \quad (b) \quad (9)$$

where the zero value of the real part of the total admittance is enabled by the negative coefficient a . Each solution of (9) is obtained by first solving $Y_{T,i}(\omega) = 0$ for ω and then replacing its value in $Y_{T,r}(V, \omega) = 0$, which is solved for V .

In the presence of parasitic losses ($R_{pi} \neq 0$), the output power is obtained by solving the following system for I_3 and making $P_{out} = 1/2R_3|I_3|^2$:

$$\begin{aligned} (L_1 j\omega + R_{p1})I_1 + M_1 j\omega I_2 &= V \\ M_1 j\omega I_1 + \left(\frac{1}{C_2 j\omega} + L_2 j\omega + R_{p2} \right) I_2 + M_2 j\omega I_3 &= 0 \\ M_2 j\omega I_2 + \left(R_L + R_{p3} + \frac{1}{C_3 j\omega} + L_3 j\omega \right) I_3 &= 0 \end{aligned} \quad (10)$$

where V and ω are the values resulting from (9). As in Section II-A, to get analytical insight, we will initially neglect the parasitic losses, so the transferred power can be expressed in terms of $Y_{in,r}$. We will first solve $Y_{T,r}(V, \omega) = 0$ for V^2 , which provides

$$V^2 = \frac{-Y_{in,r} - a}{\beta}. \quad (11)$$

Then, the output power is

$$P_{out} = \frac{1}{2} Y_{in,r} \frac{(-Y_{in,r} - a)}{\beta} = -\frac{1}{2} \frac{Y_{in,r}^2 + a Y_{in,r}}{\beta}. \quad (12)$$

As in the dc stability analysis, we will assume that $k_2 = 0.2$ and obtain the oscillator response versus k_1 . Note that lower k_2 values will be considered later in this section. Fig. 4 presents the solution curves in terms of P_{out} and ω versus k_1 . There are two distinct curves, each corresponding to one of the two different oscillation modes (MD1 and MD2), already detected in the dc stability analysis. The mode MD1 (which departs from $k_1 = 0$) exists for any k_1 . Its frequency departs from $f_1 = 13.56$ MHz at $k_1 = 0$ [Fig. 4(b)] and undergoes a slight decrease versus k_1 . The maximum transferred power is $P_{out,max} = 1.67$ mW [Fig. 4(a)]. On the other hand, the mode MD2 arises from the direct Hopf bifurcation H_1 [34], [35], [39] occurring at $k_{H1} = 0.221$ (already detected in Fig. 2). The mode MD2 departs from the frequency $f_2 = 15.27$ MHz [Fig. 4(b)] and reaches $f_2 = 60.13$ MHz at the inverse Hopf bifurcation H_2 , where this mode vanishes. Thus, it exhibits a significant frequency variation. For MD2, there are two k_1 values enabling maximum transferred power $P_{out,max} = 1.67$ mW. As shown in Section II-C, MD1 is fully stable, and MD2 stabilizes from a certain k_1 .

The results of the analytical formulation have been validated with HB at the fundamental frequency. A default HB oscillator analysis (red squares) only provides mode MD1. It is unable to detect the existence of MD2. To obtain mode MD2, we have made use of the auxiliary-generator (AG) technique [34], [38]. The AG is a voltage source [Fig. 1(a)] operating at the oscillation frequency ω with the amplitude V , in series with an ideal bandpass filter at ω . The AG must fulfill a

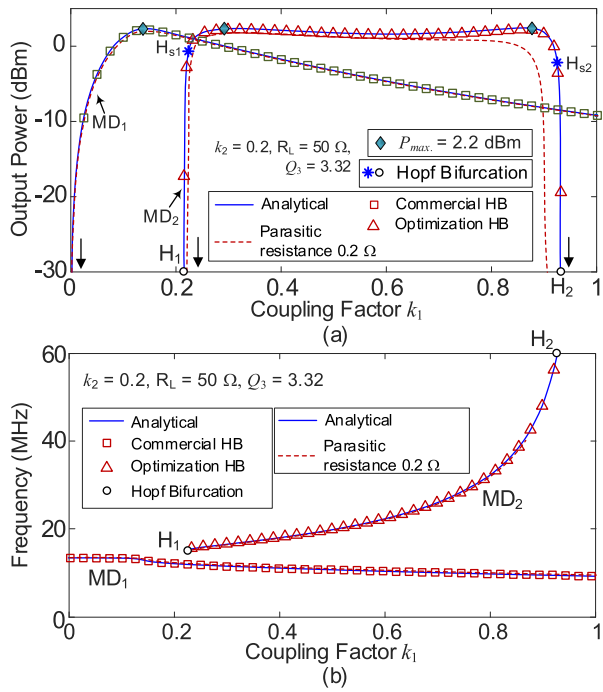


Fig. 4. Analysis of the cubic-nonlinearity oscillator in Fig. 1 under $k_2 = 0.2$. The quality factor of the receiver resonator is $Q_3 = 3.32$. The results of the analytical formulation are compared with HB at the fundamental frequency. Default HB is indicated with red square markers and AG optimization is indicated with triangles. The solution curves when considering the loss resistor $R_{p2} = 0.2 \Omega$ are also superimposed. (a) Power transferred to the load resistor R_L versus k_1 . (b) Oscillation frequency versus k_1 .

nonperturbation condition [34], [38], given by the zero value of the ratio between its current and voltage, which is achieved through an optimization procedure. For the analysis of the circuit in Fig. 1(a), we have introduced the AG in parallel with the nonlinear element. To obtain the top section of the MD2 curve (triangles), we have swept k_1 and optimized the AG amplitude and frequency ω . To obtain the two high-slope sections, we have swept the AG amplitude and optimized k_1 and ω . In the two cases (default HB and AG-based HB), the results are overlapped with those obtained with the analytical formulation.

We have compared the above results with those obtained in the presence of parasitic losses, using (10) to calculate the output power. The results when assuming the loss resistor $R_{p2} = 0.2 \Omega$, in the order of the values considered in [43] and [44], are represented in Fig. 4. The loss resistor mainly affects the second maximum of the undesired mode MD2, at a relatively high k_1 . The oscillation frequency is nearly overlapped.

C. Stability Analysis of the Periodic Modes

To be physically observable, the periodic oscillation must be stable. This means that under any small perturbation, the system will return exponentially in time to this solution [34], [38]. To fulfill this condition, all the poles resulting from the system linearization about the periodic oscillation must be in the LHS of the complex plane, except those associated with the oscillation autonomy, given by $\pm jm\omega_0$, where ω_0 is the oscillation frequency and m is an integer.

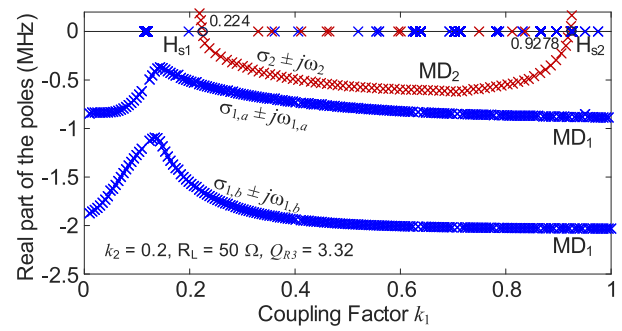


Fig. 5. Stability analysis through pole-zero identification of the two periodic modes of the cubic-nonlinearity oscillator in Fig. 1(a). MD1 (blue) and MD2 (red). Variation of the real part of the dominant poles versus k_1 for $k_2 = 0.2$.

In uncoupled operation ($k_1 = 0$), the periodic solution of the cubic-nonlinearity oscillator is stable, as demonstrated in many previous works [32], [33], [34], [35]. Thus, it will remain at least up to a certain k_1 . On the other hand, mode MD2 arises at the Hopf bifurcation H_1 [34], [38], [39] from an unstable dc solution, as shown in Fig. 2. As a result, MD2 will be unstable in the neighborhood of H_1 , to comply with the bifurcation relationships [39]. This is confirmed by the rigorous stability analysis of the two oscillation modes presented in the following.

The stability of the two periodic modes will be analyzed through pole-zero identification [41], [42], which relies on the fact that all the transfer functions that can be defined in a linear system share the same denominator. The circuit in Fig. 1 will be linearized about each periodic solution by connecting a small-signal current source at the perturbation frequency Ω to node n_v . The transfer function to be identified is obtained through the conversion-matrix approach [41], [42] as the ratio between the node voltage at Ω and the current of the small-signal source. This transfer function is fit with a quotient of polynomials. In Fig. 5, the real part of the poles associated with the two modes is traced versus k_1 . Note that for each of the two modes, there is always a pair of complex-conjugate poles on the imaginary axis (zero real part), associated with the oscillation autonomy. For MD1 (real part in blue), we obtain two other pairs of complex-conjugate poles ($\sigma_{1,a} \pm j\omega_{1,a}$ and $\sigma_{1,b} \pm j\omega_{1,b}$) at incommensurate frequencies with negative real parts for all the k_1 values. Thus, this mode is always stable. On the other hand, MD2 (real part in red) is initially unstable with a pair of complex-conjugate poles, $\sigma_2 \pm j\omega_2$, about the frequency of MD1 having a positive real part. However, this pair of poles crosses the imaginary axis to the LHS at the inverse secondary Hopf bifurcation H_{s1} [35], [39], where MD2 becomes stable. “Secondary” indicates that the bifurcation takes place from a periodic regime instead of a dc one. The mode MD2 becomes unstable again at the direct secondary Hopf bifurcation H_{s2} , where the pair $\sigma_2 \pm j\omega_2$ crosses again to the RHS. In view of the results in Fig. 5, MD2 is stable for a large range of k_1 values. If k_1 is gradually increased from zero, we will observe MD1. Due to the continuous stability of MD1, observing MD2 will require a relatively large perturbation. Note that in the presence of nonlinearities of higher order

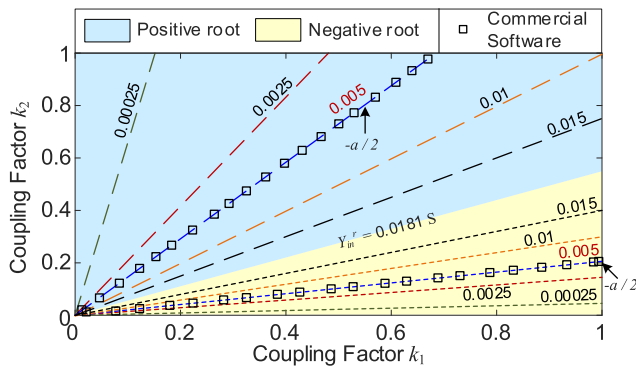


Fig. 6. Loci of constant $Y_{in,r}$ (going from 0.25 to 15 mS) at the frequency $f_0 = 13.56$ MHz (agreeing with the resonance frequency of the two resonators), traced in the plane defined by k_1 and k_2 .

[45], [46], [47], together with the coexistent periodic modes, there can be stable quasi-periodic solutions.

D. Dependence of the Input Conductance $Y_{in,r}$ on k_1 and k_2

As already stated, in the absence of parasitic losses, the transferred power is fully determined by $Y_{in,r}$ [see (12)]. Thus, it will be of interest to analyze the dependence of $Y_{in,r}$ on k_1 and k_2 . To get some insight into this dependence, we will initially evaluate $Y_{in,r}$ at the desired oscillation frequency ω_0 , under the condition $\omega_2 = \omega_3 = \omega_0$. This leads to the expression

$$\begin{aligned} Y_{in,r} &= \frac{Q_3^{-1} k_1^2 k_2^2}{L_1 \omega_0 (k_2^2 + Q_3^{-2} k_1^4)} \\ &= \frac{1}{L_1 \omega_0 (Q_3 k_1^{-2} k_2^2 + Q_3^{-1} k_1^2 k_2^{-2})}. \end{aligned} \quad (13)$$

To obtain the locus of coupling factors k_1 and k_2 that provides each $Y_{in,r}$, we will solve (13) for k_2^2 in terms of k_1^2

$$k_2^2 = \frac{1 \pm \sqrt{1 - 4Y_{in,r}^2 L_1^2 \omega_0^2}}{2Y_{in,r} L_1 \omega_0} Q_3^{-1} k_1^2. \quad (14)$$

For $Y_{in,r} < (2L_1\omega_0)^{-1}$, the locus is composed of two straight lines with different slopes, corresponding to the two different signs before the square root. The slopes depend on the nondimensional quantity $Y_{in,r} L_1 \omega_0$ and the quality factor of the receiver resonator Q_3 . Fig. 6 presents the loci corresponding to values of $Y_{in,r}$ going from 0.25 to 15 mS. The results of (14) have been validated with a commercial simulator, performing a double sweep in k_1 and k_2 and calculating the contours of constant $Y_{in,r}$. Note the high sensitivity for small values of k_1 and k_2 . Note that if the drive frequency ω_0 is different from $\omega_2 = \omega_3$, the loci of constant $Y_{in,r}$ are no longer straight lines. From a different viewpoint, by inspecting the results in Fig. 6, one can deduce that under a constant drive frequency $\omega_0 = \omega_2 = \omega_3$ and any linear relationship between k_2 and k_1 , the coupled network will exhibit a constant $Y_{in,r}$.

E. Maximum Transferred Power

Neglecting losses in the coupling network, the maximum transferred power $P_{out,max}$ is obtained from an extremum cal-

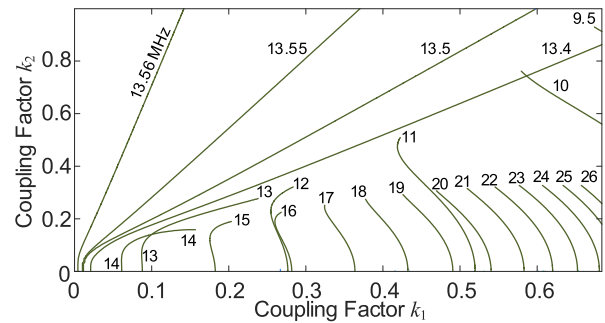


Fig. 7. Contours of constant steady-state oscillation frequency ω , obtained from the roots of $Y_{T,i}(\omega, k_1, k_2)$ fulfilling $Y_{T,r}(\omega, k_1, k_2) = 0$, traced in the plane defined by k_1 and k_2 .

ulation, by making

$$\frac{\partial P_{out}}{\partial Y_{in,r}} = -\frac{1}{2} \frac{2Y_{in,r} + a}{\beta} = 0 \quad (15)$$

which provides $Y_{in,r} = -a/2$. Replacing this value in (12), we obtain

$$P_{out,max} = a^2/6b. \quad (16)$$

In the oscillator, $Y_{in,r}$ must be evaluated at the frequency that fulfills $Y_{T,i}(\omega, k_1, k_2) = 0$. This equation is too complex to derive an analytical expression for $\omega(k_1, k_2)$. Instead, we will trace the set of constant oscillation-frequency contours in the plane defined by k_1 and k_2 . A double sweep is performed in k_1 and k_2 and, at each sweep step, we calculate the roots of $Y_{T,i}(\omega, k_1, k_2)$ fulfilling $Y_{T,r}(V, \omega, k_1, k_2) = 0$. The results are shown in Fig. 7. As can be seen, from certain k_2 , no matter the k_1 value, the oscillation frequency is close to the common resonance frequency $\omega \cong \omega_2 = \omega_3$ ($f = 13.56$ MHz). When this happens, the loci of constant oscillation frequency are given by straight lines (see, for instance, the ones comprised between 13.4 and 13.56 MHz). On the other hand, the larger frequency values correspond to MD2, in consistency with the resonance analysis of Fig. 3(b).

For k_2 above a certain value ($k_2 \cong 0.1$, in the case of the circuit analyzed here), when following any straight line $k_2(k_1)$, the oscillation frequency will be close to $\omega_2 = \omega_3$ ($f = 13.56$ MHz), as shown in Fig. 7. Assuming that $\omega = \omega_0$, the relationship $k_2(k_1)$ providing $P_{out,max}$ will be obtained by replacing $Y_{in,r} = -a/2$ in (14). This leads to the expression

$$k_2^2 = \frac{-1 \pm \sqrt{1 - a^2 L_1^2 \omega_0^2}}{a L_1 \omega_0} Q_3^{-1} k_1^2. \quad (17)$$

For $1 - a^2 L_1^2 \omega_0^2 > 0$, the locus of transferred-power maxima is given by two straight lines. The slope of k_2 versus k_1 increases with $Q_3^{-1} = (R_L / (L_3 \omega_0))$, and, thus, with R_L . Therefore, when increasing R_L for the same k_1 , we will need a higher k_2 to reach the maximum output power. Note that k_1 and k_2 , respectively, depend on the distances d_1 and d_2 between the first and the second inductor, and between the second and the third one. By increasing Q_3 , we will have $P_{out,max}$ at a larger d_2 and a smaller d_1 . This result is consistent with the findings in [19], where instead of a full oscillatory system,

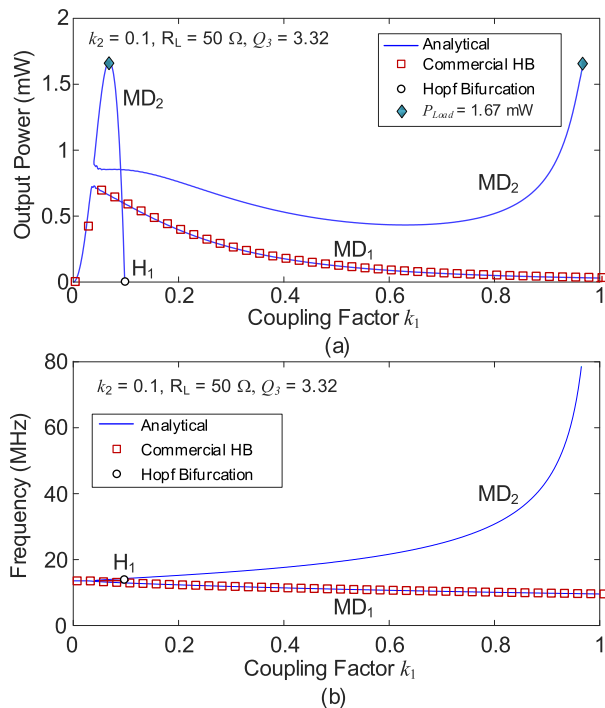


Fig. 8. Analysis of the cubic-nonlinearity oscillator in Fig. 1(a) under $k_2 = 0.1$. There are two oscillation modes: MD1 and MD2. Default HB results are indicated with red square markers. (a) Power transferred to the load resistor versus k_1 . (b) Oscillation frequency versus k_1 .

three coupled resonators driven by an independent source were considered. As has been verified, for very small k_1 , the maximum is just a mathematical solution without physical existence, corresponding to the unstable mode MD2. This can be seen in the solution curves, obtained for $k_2 = 0.1$, presented in Fig. 8. In practice, for very small k_2 and k_1 , it will be very difficult to ensure that $Y_{in,r} = -a/2$ due to the high sensitivity to the loci in Fig. 6.

The condition (17) has been verified by imposing the relationship $k_2(k_1)$ in both our in-house software [using (9)] and commercial HB. We have swept k_1 and obtained k_2 from (17) at each sweep step. The results in terms of output power and frequency are shown in Fig. 9. We also obtain two modes. In agreement with Fig. 8, the mode MD2 is the one that provides a high output power under small k_1 and k_2 , and in these conditions, it is unstable. In turn, mode MD1 reaches a power value close to the maximum (Fig. 9) when its frequency reaches a value close to ω_0 . As deduced from Fig. 7, a linear relationship between k_1 and k_2 facilitates a constant oscillation frequency. Moreover, because we are moving along a straight line $k_2(k_1)$, we have a constant value of $Y_{in,r}$, in agreement with Fig. 6. Due to the specific relationship (17), (where $Y_{in,r} = -a/2$), the output power will be close to $P_{out,max}$. It would be exactly $P_{out,max}$ if the oscillation frequency fully agreed with ω_0 . As stated, the results have been validated with commercial HB, which is only able to detect MD1. The curves obtained with (9) and commercial HB are overlapping. The output power is very close to $P_{out,max}$, which demonstrates the validity of expression (17).

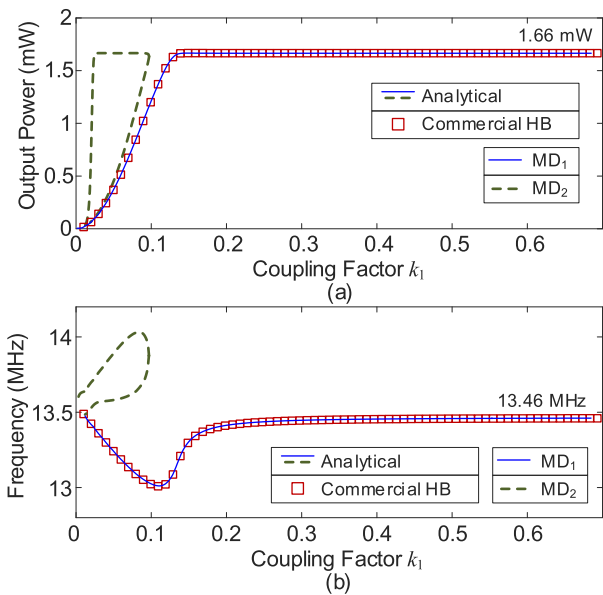


Fig. 9. Validation of condition (17) in both in-house software and commercial HB. The coupling factor k_1 is swept and, at each sweep step, k_2 is obtained from (17). (a) Output power. (b) Oscillation frequency.

We have also carried out a general evaluation of the transferred power versus k_1 and k_2 . With this aim, we have performed a double sweep in k_1 and k_2 . For each point of the sweep, we make use of (9) and (12) to obtain the output power. This provides the surface $P_{out}(k_1, k_2)$ shown in Fig. 10, where a color gradient has been used to indicate the different output-power levels. There are two distinct regions, as expected from the existence of the two distinct modes MD1 and MD2. The contour plot corresponding to $P_{out} = 1.667$ mW (slightly smaller than $P_{out,max}$) has been represented in a dotted line and the two straight lines in (17) have also been traced. The straight line with positive sign provides the maximum output power. Note that it lies within the contour $P_{out} = 1.667$ mW. In contrast, the straight line with negative sign does not provide the maximum output power. This is because, through this line, the oscillation frequency is quite different from $\omega = \omega_0$.

III. TRANSISTOR-BASED OSCILLATOR

In this section, we will analyze the behavior of a practical Class-E oscillator [Fig. 11(a)]. This oscillator is coupled to an intermediate resonator that is, in turn, coupled to a receiver one in a series configuration. The Class-E oscillator is based on a commercial MOSFET with reference IRLML0040TRPbF. For the oscillator design, we have followed the procedure described in [27]. We have initially obtained a Class-E amplifier at $f_0 = 13.56$ MHz (with no series feedback) by selecting the values of the output-network elements (C_D , C_1 , and L_1) that fulfill the zero-voltage switching (ZVS) condition. Note that the capacitor C_g is a dc block and the inductor L_{dc} is a dc feed. In coupled conditions, we have calculated the drain efficiency as the ratio between the power delivered to R_L and the drain power consumption: $\eta = P_{out}/P_{dc}$, where $P_{dc} = V_{dc}I_{dc}$. Note that the transistor load impedance depends on the factors k_1 and k_2 and, thus, on the distances between

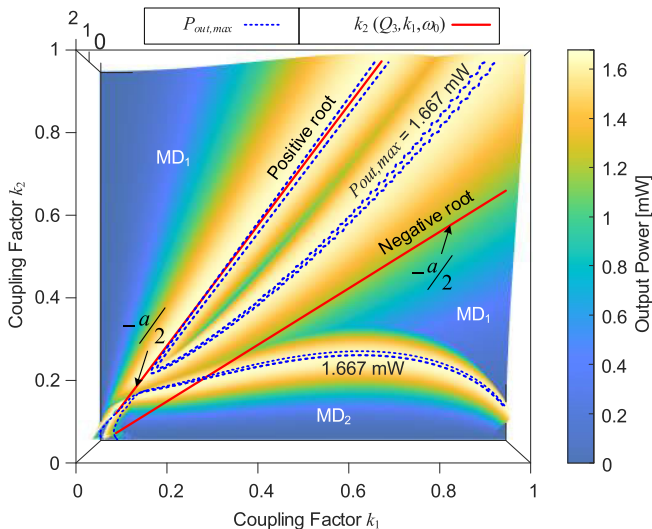


Fig. 10. General variation of the oscillation output power versus k_1 and k_2 , obtained from (9) and (12). A color gradient has been used to indicate the different output-power levels. The contour plot corresponding to $P_{\text{out}} = 1.667$ mW (slightly smaller than $P_{\text{out,max}}$) has been represented in the dotted line. The straight lines given by (17) have also been traced.

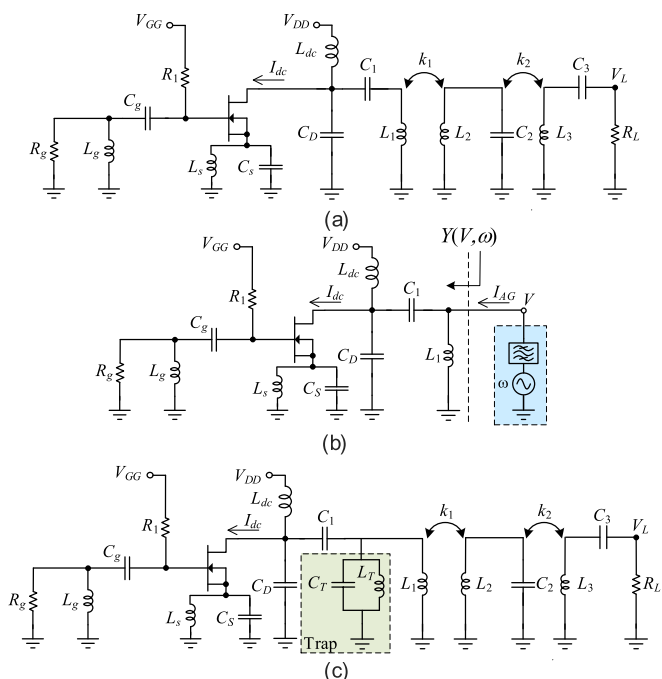


Fig. 11. Class-E power oscillator coupled to an intermediate resonator that is, in turn, coupled to a receiver one, in a series configuration. (a) Schematic. The component values are: $R_g = 10 \Omega$, $C_g = 1 \mu\text{F}$, $C_3 = 7 \text{ nF}$, $C_D = 43.29 \text{ pF}$, $C_1 = 58.55 \text{ pF}$ (original), $C_1 = 120 \text{ pF}$ (reoptimized), $C_3 = 53 \text{ pF}$, $C_2 = 48.54 \text{ pF}$, $L_g = L_s = 100 \text{ nH}$, $L_{dc} = 15 \mu\text{H}$, $L_1 = L_3 = 2.6 \mu\text{H}$, $L_2 = 2.84 \mu\text{H}$, $R_1 = 1.5 \text{ k}\Omega$, and $R_L = 50 \Omega$. (b) Connection of an AG to obtain the nonlinear admittance function $Y(V, \omega)$ that describes the oscillator's active core. (c) Schematic including a trap resonator to suppress the undesired oscillation modes.

the coils. As a result, the variation of k_1 and k_2 will have an impact on the voltage and current waveforms and, therefore, on the ZVS conditions. This problem is general to all power transfer systems based on Class-E amplifiers or oscillators. For the input power $P_{\text{in}} = 14.35 \text{ dBm}$, when performing a

double sweep in k_1 and k_2 , the maximum efficiency is obtained for $k_1 = 0.25$ and $k_2 = 0.1$ and it corresponds to $\eta \cong 84\%$. Following the method in [27], the amplifier is transformed into a free-running oscillator at $f_0 = 13.56 \text{ MHz}$ by introducing the series-feedback capacitor C_S , in parallel with the dc feed L_S , and suitably choosing the gate termination elements.

A. Oscillation Modes

The previous analytical section has demonstrated the potential complexity of the circuit solutions, which may involve the coexistence of distinct periodic oscillation modes. An exhaustive calculation of these modes will be essential to accurately predict the system behavior. For this exhaustive calculation, we will make use of an extension of the semianalytical formulation presented in [27] and [28]. In this formulation, the oscillator active core is described with a nonlinear admittance function, $Y(V, \omega)$, extracted from HB simulations with the aid of a voltage AG, operating at the fundamental frequency ω , with the amplitude V [Fig. 11(b)]. The function $Y(V, \omega)$ is obtained through a double sweep in ω and V , calculating the ratio between the AG current I_{AG} (entering the circuit) and the delivered voltage V , that is, $Y(V, \omega) = I_{\text{AG}}/V$. Although $Y(V, \omega)$ is extracted at the fundamental frequency, in the HB simulation carried out for its extraction, we consider as many harmonic terms ($\text{NH} = 7$) as required for an accurate representation of the device's intrinsic variables. In contrast, inductive coupling is considered at the fundamental frequency only. We disregard the inductive coupling at the harmonic terms, which is enabled by the low-pass filtering effects of the oscillator output. At each point of the double sweep, we also extract the dc current I_{dc} [see Fig. 11(a)], which will be used to calculate the drain efficiency as $\eta = P_{\text{out}}/P_{dc}$. With the above considerations, the steady-state solutions of the coupled oscillator are obtained from the following equation:

$$Y_T(V, \omega) = Y(V, \omega) - \frac{1}{jL_1\omega} + Y_{\text{in}}(k_1, k_2, \omega) = 0. \quad (18)$$

Note that the function $Y(V, \omega)$ is extracted with the inductor L_1 connected to the oscillator output [Fig. 9(b)]. This is why the admittance of this inductor is subtracted in (18). To fulfill (18) $Y(V, \omega)$ must exhibit a negative conductance in a certain frequency band of about ω_0 , as ensured by the original oscillator design. For the passive linear admittance $Y_{\text{in}}(k_1, k_2, \omega)$, we can use the analytical expression in (4) or a more realistic description, which would be calculated separately and introduced in (18).

Equation (18) is solved through a contour-intersection procedure. We obtain the zero-value contour of the real part $Y_{T,r}(V, \omega) = 0$ and the zero-value contour of the imaginary part $Y_{T,i}(V, \omega) = 0$. Then, all the coexisting periodic solutions are given by the intersections of the two contours.

When applying (18) for $k_2 = 0.25$ versus k_1 one obtains the results in Fig. 12, which shows the variation of the output power [Fig. 12(a)] and the oscillation frequency [Fig. 12(b)]. As deduced from the figure, there are three distinct oscillation modes.

As in Section II, in the transistor-based oscillator (Fig. 12), the mode MD1 evolves from the free-running oscillation

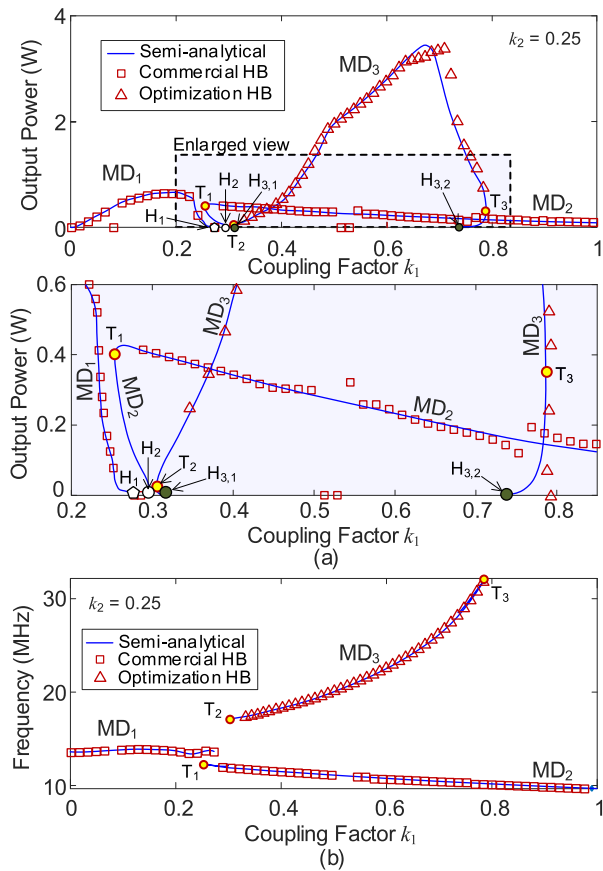


Fig. 12. Periodic solutions of the Class-E oscillator in Fig. 11(a) for $k_2 = 0.25$, calculated through (18) and traced versus k_1 . They have been validated with full HB (NH = 7 harmonic terms), considering the coupling at all the harmonic terms. The HB results of the mode MD3 are obtained through AG optimization. (a) Output power. (b) Oscillation frequency.

obtained in uncoupled conditions ($k_1 = 0$) and is extinguished at the inverse Hopf bifurcation H_1 , occurring for $k_1 = 0.27$. Its frequency departs from $f_1 = 13.56$ MHz at $k_1 = 0$ and remains about this value until it vanishes at H_1 . At H_2 (occurring at $k_1 = 0.29$), a second mode MD2 arises in a subcritical Hopf bifurcation [35], [39]. This means that the solution curve corresponding to MD2 goes backward and exhibits the turning point T_1 . The upper and lower sections of the curve (before and after T_1) are nearly overlapping [Fig. 12(c)]. Thus, two modes MD1 and MD2 coexist in the k_1 interval 0.25–0.27. Mode MD2 is not extinguished versus k_1 ; its frequency is smaller than that of MD1 and decreases with k_1 up to 10 MHz. At the direct Hopf bifurcation $H_{3,1}$, occurring at $k_1 = 0.3$, a third mode (MD3) arises at the frequency $f_3 = 17.13$ MHz. This mode has much higher power (and low efficiency for most k_1 values) because of the circuit operation at quite a different frequency. It is extinguished at the inverse Hopf bifurcation $H_{3,2}$, occurring at $k_1 = 0.73$. Mode MD3 exhibits the turning points T_2 and T_3 . Modes MD2 and MD3 coexist in a large k_1 interval.

The predictions of (18) have been verified with full HB using NH = 7 harmonic terms (thus considering the coupling effects at all the harmonic terms) and the results are superimposed in Fig. 12 with excellent agreement. Default HB provides relatively large sections of the curves corresponding

to MD1 and MD2. However, it fails to provide any solutions in some k_1 intervals. On the other hand, mode MD3 has been obtained through AG optimization [34], [38]. Note that in the case of MD3, there is a slight discrepancy with the AG-based HB results because, in (18), we neglect the coupling at higher harmonic terms. One should emphasize that (18), solved through the contour-intersection method, simultaneously provides all the solutions coexisting for each k_1 .

In the practical transistor-based design, the undesired oscillation modes must be suppressed. This will be done with the aid of a trap resonator connected to the output of the active core, as shown in Fig. 11(c). The effect of the trap resonator can be analyzed by including its admittance in the system equation at the fundamental frequency

$$Y(V, \omega) - \frac{1}{jL_1\omega} + Y_{\text{trap}}(\omega) + Y_{\text{in}}(k_1, k_2, \omega) = 0$$

$$Y_{\text{trap}}(\omega) = jC_{\text{trap}}\omega + \frac{1}{jL_{\text{trap}}\omega}. \quad (19)$$

In the above equation, the nonlinear admittance function $Y(V, \omega)$ is the same one used in (18). Equation (19) enables a flexible and computationally efficient selection of the trap element values. However, when introducing the trap, a reoptimization of the oscillator's active core might be convenient. This reoptimization leads to the new value $C_1 = 120$ pF with the trap-resonator elements: $L_{\text{trap}} = 20$ nH and $C_{\text{trap}} = 6.84$ nF. For better accuracy, we have recalculated $Y(V, \omega)$ with L_{trap} and C_{trap} absorbed by the active core. Thus, under variations in the coupled-resonator parameters, the oscillator will be analyzed with (18). The solution curves obtained for $k_2 = 0.1$ and $k_2 = 0.25$ are shown in Fig. 13. They are validated with full HB with NH = 7 (considering the coupling effects at all the harmonic terms) with excellent agreement. As can be seen, the undesired modes MD2 and MD3 are fully suppressed, and MD1 exists for all k_1 values. In Fig. 13(c), the output power is compared with the one obtained when including the parasitic resistances of the three inductors. The value $R_{pi} = 0.56 \Omega$, obtained through an experimental characterization of the coils, has been considered. As expected, the loss resistances give rise to a small reduction in output power [Fig. 13(c)]. On the other hand, the oscillation frequency is nearly overlapping.

Besides the suppression of the undesired modes, a benefit of the trap is the reduction in the oscillation-frequency variations. To verify this, we have performed a double sweep in k_1 and k_2 and calculated for each pair of values (k_1, k_2) the steady-state solution(s), in terms of V and ω , using (18). Then, we have obtained the constant oscillation-frequency contours, as shown in Fig. 14. Due to the trap, the steady-state oscillation frequency remains close to ω_0 for most of the plane k_1 and k_2 . Only the contour corresponding to the precise value of the uncoupled free-running frequency reaches the point (0, 0). Note that the calculation of constant oscillation-frequency loci would be virtually impossible in full HB due to the huge computational cost. Here, this calculation is enabled by the semianalytical formulation (18).

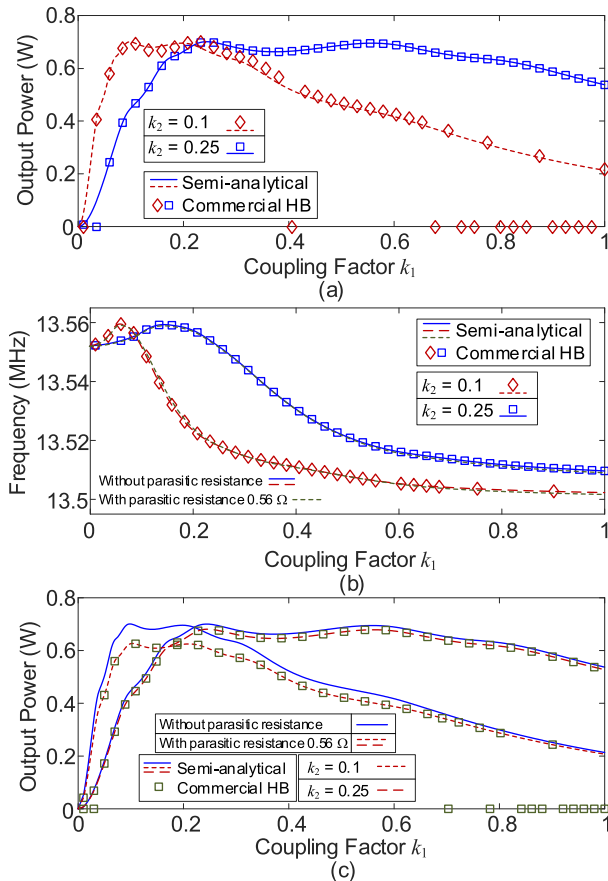


Fig. 13. Application of (18) to the Class-E oscillator in the presence of the trap resonator for the coupling factors $k_2 = 0.1$ and $k_2 = 0.25$. The solutions are traced versus k_1 . They have been validated with full HB (NH = 7 harmonic terms), considering the coupling at all the harmonic terms. The impact of the inductor losses is also analyzed. The loss resistances are $R_{pi} = 0.56 \Omega$, where $i = 1-3$. (a) Output power. (b) Oscillation frequency with and without losses. (c) Effect of the inductor losses on the output power.

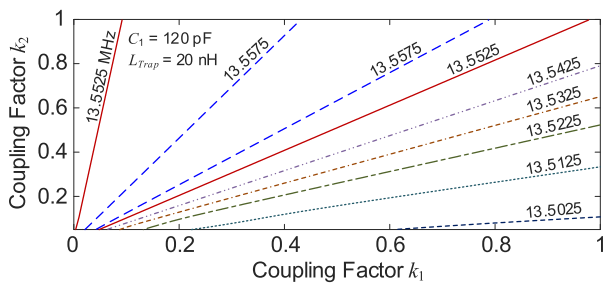


Fig. 14. Constant steady-state oscillation-frequency contours of the circuit in Fig. 11(a) in the presence of the trap resonator.

B. Oscillator-Core Capabilities for Power Delivery

In Section II, it was possible to analytically derive the oscillator's maximum output power due to the availability of an explicit function $Y_N(V)$. In (20) (corresponding to the practical oscillator), we do not have analytical expressions for the real and imaginary parts of $Y(V, \omega)$, which both depend on the excitation amplitude V and frequency ω . In this situation, to obtain the maximum output power, we will make use of a new numerical procedure, valid under negligible parasitic loss.

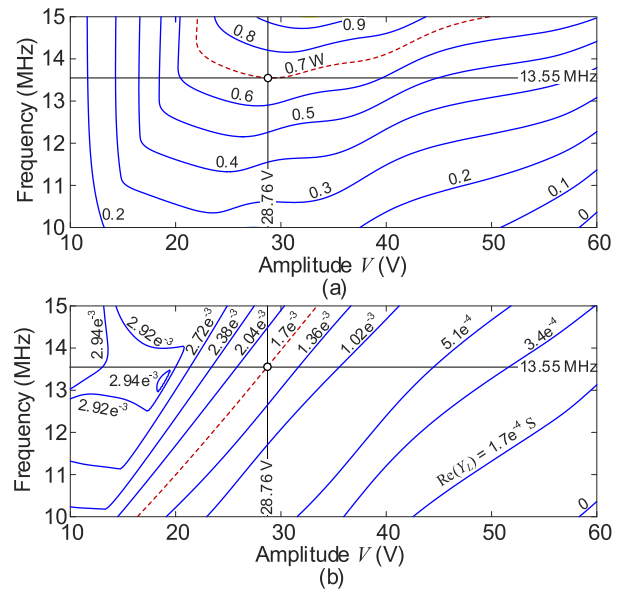


Fig. 15. Contours of “available” oscillator power obtained from (20), using the nonlinear function $Y(V, \omega)$, extracted from HB. (a) Available power in the plane defined by V and ω . (b) Contours of constant $Y_{in,r} = -\text{Re}[Y(V, \omega)]$ traced in the same plane.

We will first analyze the capabilities for power delivery of the oscillator core, making use of the nonlinear function $Y(V, \omega)$, which will include the trap. Neglecting, as stated, the parasitic loss, for each pair (V, ω) , the “available” oscillator power is

$$P_{\text{Out,av}} = -\frac{1}{2} \text{Re}[Y(V, \omega)] V^2. \quad (20)$$

To obtain a steady-state oscillation with a given value of $P_{\text{Out,av}}$, we should introduce a passive linear load Y_{in} that fulfills

$$Y(V, \omega) + Y_{in}(\omega, k_1, k_2) = 0. \quad (21)$$

We will first trace contours of constant $P_{\text{Out,av}}$ in the plane defined by ω and V , using the already extracted function $Y(V, \omega)$, as well as the corresponding AG amplitude V . These contours are shown in Fig. 15(a). For the specific frequency $f_0 = 13.55$ MHz, the maximum output power, corresponding to $P_{\text{Out,max}} = 0.7$ W, is obtained for $V = 28.76$ V. We also trace the contours of constant $Y_{in,r} = -\text{Re}[Y(V, \omega)]$, as shown in Fig. 15(b). From these contours, to obtain $P_{\text{Out,max}}$ at 13.55 MHz, the circuit must be loaded with $Y_{in,r}(\omega, k_1, k_2) = Y_{in,r,\text{max}} = 1.7$ mS. As deduced from the constant-frequency loci in Fig. 14, in the presence of the trap, (21) will always provide an oscillation frequency close to the desired one ω_0 , as shown in Fig. 15. Thus, to obtain the k_1 and k_2 relationship for maximum power transfer, we will replace $Y_{in,r,\text{max}}$ in expression (14), which provides

$$k_2^2 = \frac{1 \pm \sqrt{1 - 4Y_{in,r,\text{max}}^2 L_1^2 \omega_0^2}}{2Y_{in,r,\text{max}} L_1 \omega_0} Q_3^{-1} k_1^2. \quad (22)$$

For a rigorous validation, we have introduced (14) in commercial HB. We have considered the straight line with a positive sign, although, as shown later, the one with a negative sign also provides valid solutions with high output power. This

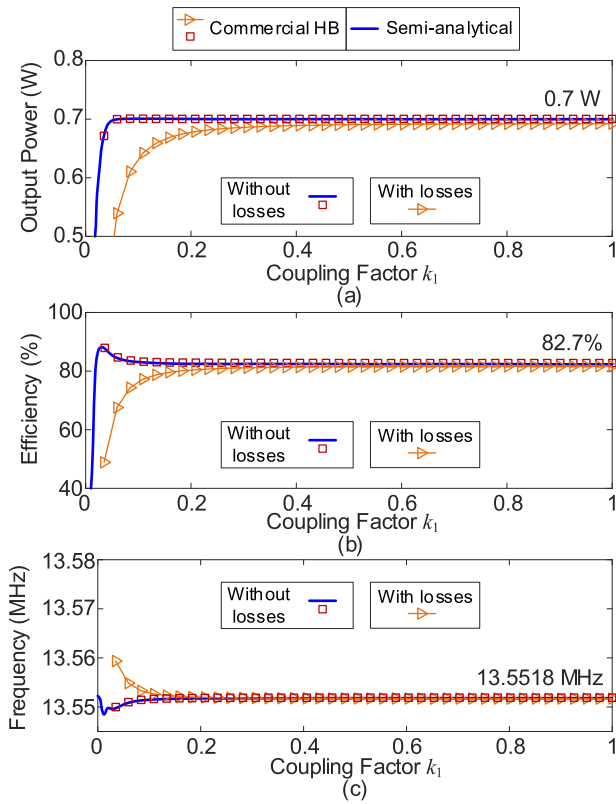


Fig. 16. Test of the validity of the relationship $k_2(k_1)$ in (22) to obtain the maximum output power. HB analysis of the complete circuit, coupled to the two external resonators, with $NH = 7$ harmonic terms. Results when considering parasitic resistors are also shown. (a) Variation of the transferred power. (b) Efficiency. (c) Oscillation frequency.

is due to the small variation of ω in the presence of the trap. The complete circuit, coupled to the two resonators, is simulated through an oscillator analysis with $NH = 7$ harmonic terms. We have swept k_1 and obtained k_2 through (22) for each sweep step. The resulting variations of the transferred power, efficiency, and oscillation frequency are shown in Fig. 16. For too small k_1 and k_2 , it is not possible to obtain the maximum power due to the high sensitivity of $Y_{in,r}$, in agreement with Fig. 14. We have also tested the impact of the parasitics by repeating the HB simulation when including the parasitic resistances of the three inductors. As shown in Fig. 16, the response is very similar.

We will also carry out a general analysis of the variation of the output power versus k_1 and k_2 . With this aim, we will perform a double sweep in k_1 and k_2 and, for each point of the sweep, we will solve system (18) [with the trap included in $Y(V, \omega)$] in terms of V and ω . Then, we will calculate the transferred power through

$$P_{out} = \frac{1}{2} Y_{in,r}(\omega, k_1, k_2) V^2. \quad (23)$$

The above procedure provides the surface $P_{out}(k_1, k_2)$ presented in Fig. 17(a), where a color gradient has been used to indicate the different output-power levels. Note that such a global analysis (in a practical transistor-based oscillator) is only possible due to the computational efficiency of the semianalytical formulation (18). We have superimposed the

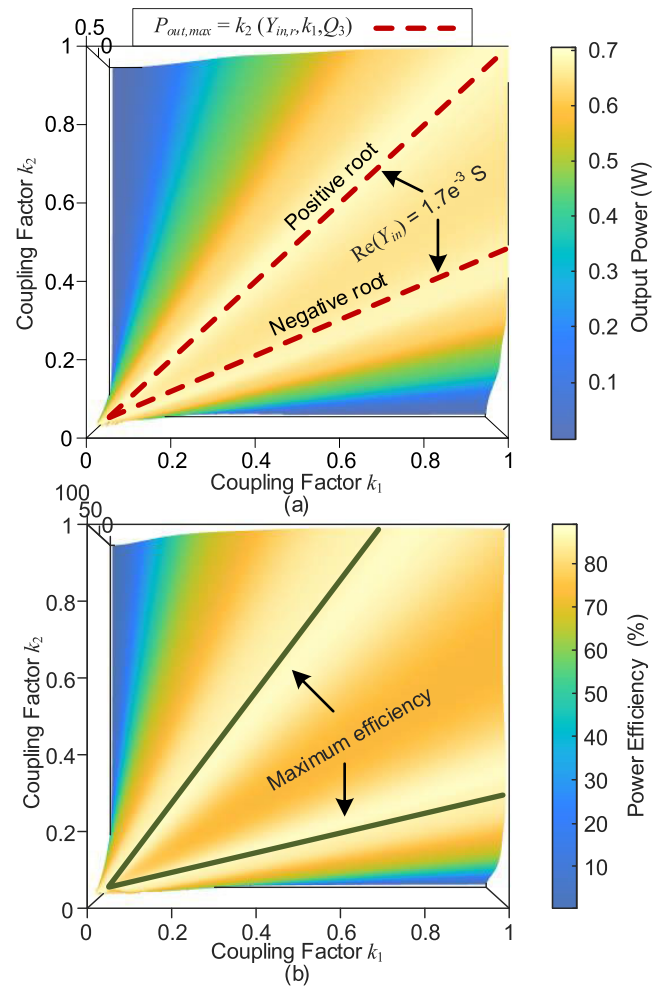


Fig. 17. General variation of the transferred power and efficiency versus k_1 and k_2 , for $C_1 = 120$ pF and the trap resonator. (a) Surface $P_{out}(k_1, k_2)$, calculated through (19) and (23), represented with a color gradient. We have superimposed the straight lines in (22), which provide the loci of power transfer maxima. (b) Efficiency surface. The two straight lines giving the maximum efficiency are superimposed.

straight lines (22) over the output-power surface. As can be seen, they define the relationship between k_1 and k_2 that provides the maximum output power. In this case, the two straight lines [corresponding to the positive and negative signs in (22)] give maxima in two different regions of the plane. This is due to the presence of the trap, which maintains the oscillation frequency nearly constant in the whole plane k_1 and k_2 (see Fig. 14). The efficiency surface is shown in Fig. 17(b). The locus of maximum values also corresponds to two straight lines.

The analysis method based on the combination of $Y(V, \omega)$ and $Y_{in}(\omega)$ can be directly extended to systems with more than two external resonators. However, one can expect even more complex behavior, due to the generation of additional oscillation modes associated with the additional resonances. As in the case of two external resonators, the additional modes can be suppressed with the aid of a trap. The optimum load admittance would be obtained through the same oscillator-power plot, proposed in this work. However, the relationship between the coupling factors required to achieve this admittance will

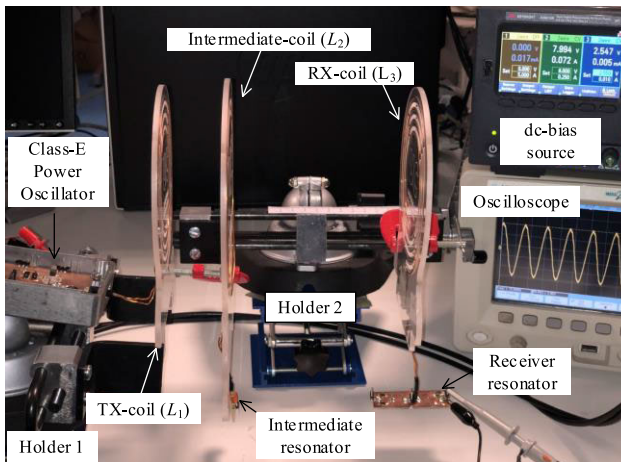


Fig. 18. Test bench for the experimental characterization of the Class-E oscillator coupled to an intermediate resonator and a receiver one. The output voltage at the receiver resonator is measured with a high-impedance probe connected to a Digital Sampling Oscilloscope DSO6034A.

depend on the number of external resonators and their specific configuration.

IV. EXPERIMENTAL RESULTS

The oscillator coupled to the two resonators has been experimentally characterized with the setup shown in Fig. 18. The output voltage at the receiver resonator is measured with a high-impedance probe connected to a Digital Sampling Oscilloscope DSO6034A, considering the effect of its parasitic capacitance. The Class-E oscillator and the intermediate and receiver resonators are implemented on the FR-4 substrate ($h = 1.6$ mm). The coils are built with AWG18 copper wound on machined acrylic sheets. The three coils have approximately the same inductance value, $L = 2.68$ μ H. The external diameter is $D_{\text{out}} = 12.53$ cm and the internal one is $D_{\text{in}} = 7.1$ cm. The number of turns is $n = 4$, and the spacing between turns is $s = 0.85$ cm. The intermediate and external coils are clamped to the jaws of a vise, which permits a more controlled variation of their separation by turning the handle. The distance d_1 between the transmitter and intermediate coils corresponding to each k_1 and the distance d_2 between the intermediate and receiver coils corresponding to each k_2 have been estimated from the measurements of the scattering parameters [48], [49].

Fig. 19(a) presents the experimental surface of output power in terms of d_1 and d_2 . In agreement with the simulations, it exhibits two local maxima, although the output power in one of them is larger than in the other. Undesired behaviors (indicated in the figure) are obtained for some distance values, which may correspond to an oscillation extinction or to the observation of a quasi-periodic solution. An example can be seen in Fig. 20, which shows the voltage waveform at the resistor of the receiver resonator. To stabilize the oscillatory system, we have introduced the trap resonator (in parallel with the coupled inductor L_1) considered in Section III-A. The trap suppresses all the undesired behaviors, at the expense of a reduction of output power [Fig. 19(b)].

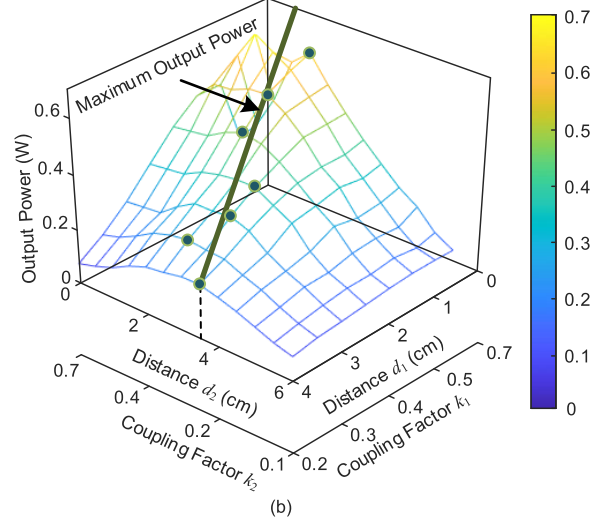
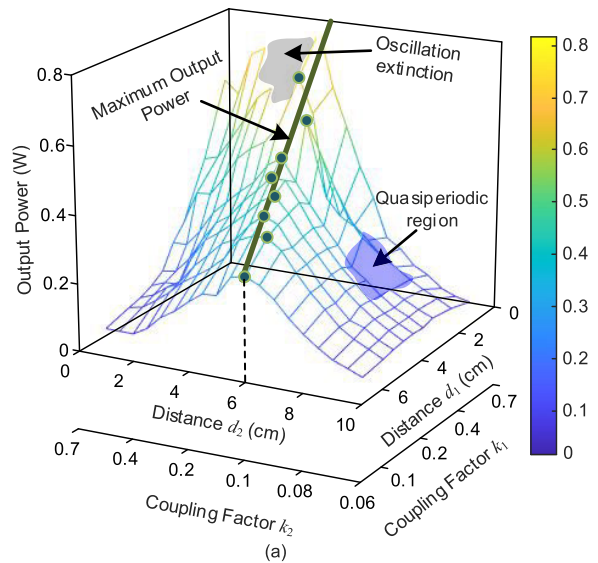


Fig. 19. Experimental surface of output power. (a) Without the trap resonator. Regions with undesired behavior are indicated. (b) With the trap resonator.

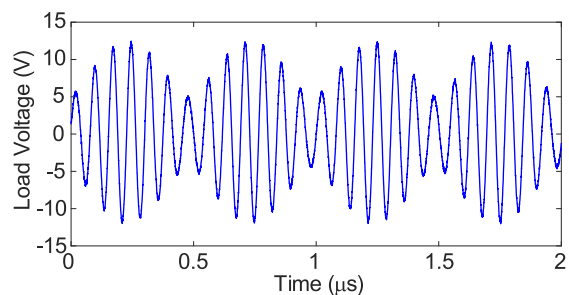


Fig. 20. Experimental quasi-periodic waveform obtained for $d_1 = 3.5$ cm and $d_2 = 5$ cm.

Fig. 21 presents the simulated and measured results versus the distance d_2 , for $d_1 = 3$ cm, in the presence of the trap. The solution curves with and without inductor losses are compared. They are both validated with default HB. The measurements of output power and oscillation frequency are represented with squares. For comparison, measurements

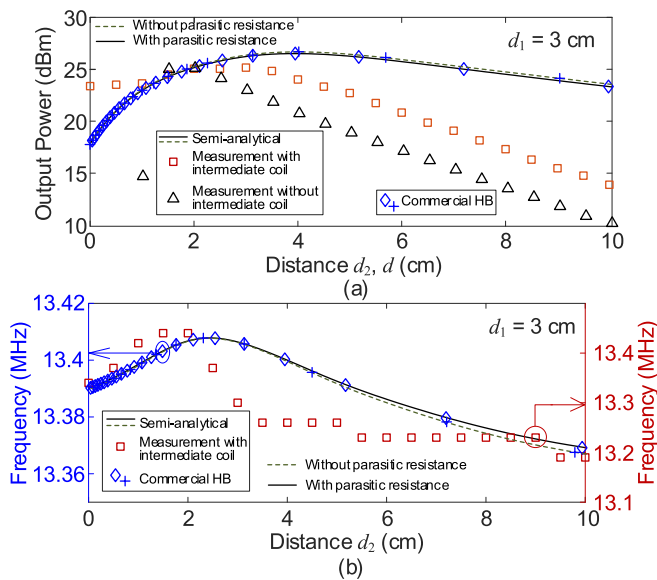


Fig. 21. Operation with the trap. Simulations and measurements versus the distance d_2 , for $d_1 = 3$ cm. Solution curves with and without inductor losses are compared. They are both validated with default HB. Measurements with and without ($d = d_2$) the intermediate resonator are also shown. The ones with the intermediate resonator are represented with squares. The ones without the intermediate resonator, taken from [27], are represented with triangles. (a) Output power. (b) Oscillation frequency.

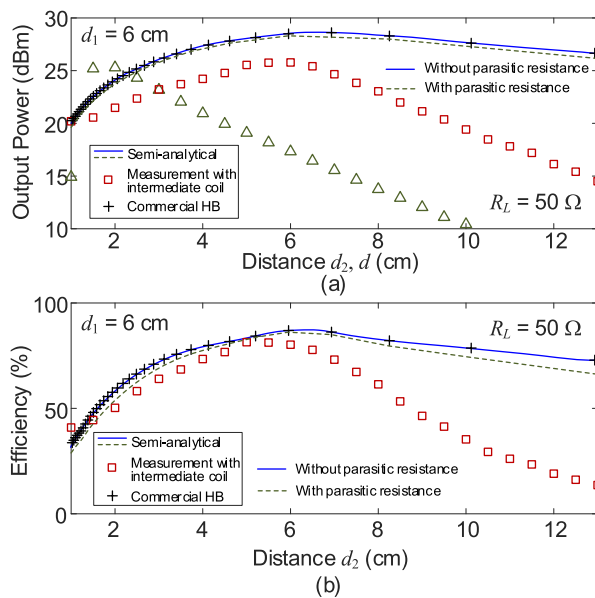


Fig. 22. Operation without the trap. Simulations and measurements versus d_2 , for $d_1 = 6$ cm. The solution curves with and without inductor losses are compared. They are both validated with default HB. Measurements with and without ($d = d_2$) the intermediate resonator are also shown. (a) Output power. (b) DC-to-RF efficiency.

without the intermediate resonator, are also shown, taken from [27] and represented with triangles. Without the intermediate resonator, the oscillation is extinguished at $d = 1$ cm, and for all the distances $d = d_2$, the transferred power is lower. Note that with the intermediate resonator, the total distance is also larger since it is given by $d_1 + d_2$. The maximum power transfer is obtained at $d_2 = 3$ cm. The frequency variations in Fig. 21(b) are small for all the d_2 values and

TABLE I
COMPARISON OF EFFICIENCY AND DISTANCE

Ref.	Driving Element	Freq. [MHz]	Efficiency (%)	Coupling factor / Distance (cm)
[15]	Oscillator	9.8–15.6	dc to RF = 80	$k_{12} = 0.16, k_{23} = 0.45$
[16]	Indep. source	4.63	RF to RF = 51.3	$d_1 = d_2 = 17.5$
[19]	Indep. source	6.78	RF to RF = 70	$d_1 = 11.5, d_2 = 25.5$
[51]	Indep. source	13.56	dc to dc = 69	$d_1 = 12, d_2 = 6$
[52]	Indep. source	5	RF to RF = 82	$d_1 + d_2 = 2$
[53]	Indep. source	13.56	RF to RF = 84.8	$d_1 = 7.4, d_2 = 0.6$
[54]	Indep. source	6.78	RF to RF = 63	$d_1 + d_2 = 23$
This work	Class-E Oscillator	13.56	dc to RF = 80.2	$d_1 = 6, d_2 = 6$

the maximum dc-to-RF efficiency is 68%. From the results of retro-simulations, we attribute the efficiency reduction to parasitics in the general-purpose capacitor of the trap resonator.

Without the trap, it is possible to reach a high efficiency at large distance between the oscillator and the receiver resonator. However, certain intervals of d_1 and d_2 must be avoided since they lead to an undesired behavior, as shown in Fig. 19(a). Fig. 22 shows the variation of the output power and efficiency for $d_2 = 6$ cm when increasing d_1 up to 12 cm. In these conditions, there are no instabilities and the maximum dc-to-RF power transfer efficiency, obtained at $d_1 = 6$ cm and $d_2 = 6$ cm, is 80.2%. The discrepancies between simulations and measurements at large distances are attributed to errors in the estimation of the small coupling factors. In Table I, we present a comparison of our experimental results with those obtained in previous works.

V. CONCLUSION

An in-depth analysis of an oscillator coupled to an intermediate resonator, which is, in turn, coupled to a receiver one, has been presented. Due to the presence of several resonances in the coupled network, the system may exhibit several oscillation modes. The undesired modes can be suppressed with the aid of a trap resonator. To maximize the power transfer, we first obtain the optimum load conductance by means of a newly proposed oscillator-power contour plot. Then, the conductance is implemented using a relationship between the coupling factors, derived in this work. The loci of maximum output power consist of two straight lines (k_2 versus k_1), whose slope decreases with the quality factor of the receiver resonator. The methods have been successfully applied to a system based on a Class-E oscillator, which has been manufactured and experimentally characterized.

REFERENCES

- [1] J. Garnica, R. A. Chinga, and J. Lin, "Wireless power transmission: From far field to near field," *Proc. IEEE*, vol. 101, no. 6, pp. 1321–1331, Jun. 2013.
- [2] S. R. Khan, S. K. Pavuluri, and M. P. Y. Desmulliez, "Accurate modeling of coil inductance for near-field wireless power transfer," *IEEE Trans. Microw. Theory Techn.*, vol. 66, no. 9, pp. 4158–4169, Sep. 2018.
- [3] L. Qian, K. Cui, H. Xia, H. Shao, J. Wang, and Y. Xia, "An inductive power transfer system for powering wireless sensor nodes in structural health monitoring applications," *IEEE Trans. Microw. Theory Techn.*, vol. 70, no. 7, pp. 3732–3740, Jul. 2022.

- [4] T. Lim and Y. Lee, "Reconfigurable coil array for near-field beam-forming to compensate for misalignment in WPT systems," *IEEE Trans. Microw. Theory Techn.*, vol. 69, no. 11, pp. 4711–4719, Nov. 2021.
- [5] D. M. Roberts, A. P. Clements, R. McDonald, J. S. Bobowski, and T. Johnson, "Mid-range wireless power transfer at 100 MHz using magnetically coupled loop-gap resonators," *IEEE Trans. Microw. Theory Techn.*, vol. 69, no. 7, pp. 3510–3527, Jul. 2021.
- [6] M. Heidarian and S. J. Burgess, "A design technique for optimizing resonant coils and the energy transfer of inductive links," *IEEE Trans. Microw. Theory Techn.*, vol. 69, no. 1, pp. 399–408, Jan. 2021.
- [7] C. Xu, Y. Zhuang, C. Song, Y. Huang, and J. Zhou, "Dynamic wireless power transfer system with an extensible charging area suitable for moving objects," *IEEE Trans. Microw. Theory Techn.*, vol. 69, no. 3, pp. 1896–1905, Mar. 2021.
- [8] K. Byron, S. A. Winkler, F. Robb, S. Vasanaawala, J. Pauly, and G. Scott, "An MRI compatible RF MEMs controlled wireless power transfer system," *IEEE Trans. Microw. Theory Techn.*, vol. 67, no. 5, pp. 1717–1726, May 2019.
- [9] H. Qiu, T. Sakurai, and M. Takamiya, "Digital transmitter coil for wireless power transfer robust against variation of distance and lateral misalignment," *IEEE Trans. Microw. Theory Techn.*, vol. 68, no. 9, pp. 4031–4039, Sep. 2020.
- [10] K. Zhang et al., "Analysis of power transfer characteristics of IPT system with near field magnetic coupling," *IEEE Trans. Electromagn. Compat.*, vol. 65, no. 6, pp. 890–899, Jun. 2023.
- [11] G. Monti, G. R. De Giovanni, M. De Liso, M. Pascali, and L. Tarricone, "Wireless power transfer strategies for medical implants: Focus on robustness and EM compatibility," *IEEE Microw. Mag.*, vol. 22, no. 9, pp. 28–41, Sep. 2021.
- [12] O. Abdelatty, X. Wang, and A. Mortazawi, "Position-insensitive wireless power transfer based on nonlinear resonant circuits," *IEEE Trans. Microw. Theory Techn.*, vol. 67, no. 9, pp. 3844–3855, Sep. 2019.
- [13] R. Chai and A. Mortazawi, "A position-insensitive wireless power transfer system employing coupled nonlinear resonators," *IEEE Trans. Microw. Theory Techn.*, vol. 69, no. 3, pp. 1752–1759, Mar. 2021.
- [14] W. X. Zhong, C. Zhang, X. Liu, and S. Y. R. Hui, "A methodology for making a three-coil wireless power transfer system more energy efficient than a two-coil counterpart for extended transfer distance," *IEEE Trans. Power Electron.*, vol. 30, no. 2, pp. 933–942, Feb. 2015.
- [15] R. Lu, M. R. Haider, and Y. Massoud, "A three-coil coupled high-efficiency power link for wireless power transfer application," in *Proc. IEEE 20th Wireless Microw. Technol. Conf. (WAMICON)*, Cocoa Beach, FL, USA, Apr. 2019, pp. 1–4.
- [16] X. Liu and G. Wang, "A novel wireless power transfer system with double intermediate resonant coils," *IEEE Trans. Ind. Electron.*, vol. 63, no. 4, pp. 2174–2180, Apr. 2016.
- [17] A. Kamineni, G. A. Covic, and J. T. Boys, "Analysis of coplanar intermediate coil structures in inductive power transfer systems," *IEEE Trans. Power Electron.*, vol. 30, no. 11, pp. 6141–6154, Nov. 2015.
- [18] X. Liu, X. Song, and X. Yuan, "Compensation optimization of the relay coil in a strong coupled coaxial three-coil wireless power transfer system," *IEEE Trans. Power Electron.*, vol. 37, no. 4, pp. 4890–4902, Apr. 2022.
- [19] K. Lee and S. H. Chae, "Power transfer efficiency analysis of intermediate-resonator for wireless power transfer," *IEEE Trans. Power Electron.*, vol. 33, no. 3, pp. 2484–2493, Mar. 2018.
- [20] J. Kim, H.-C. Son, K.-H. Kim, and Y.-J. Park, "Efficiency analysis of magnetic resonance wireless power transfer with intermediate resonant coil," *IEEE Antennas Wireless Propag. Lett.*, vol. 10, pp. 389–392, 2011.
- [21] L. R. Garcia and P. J. Abatti, "A simple method to control automatically the performance of three-coil wireless power transfer systems without direct output measurement," *Int. J. Circuit Theory Appl.*, vol. 50, no. 9, pp. 2969–2981, 2022.
- [22] A. Costanzo, F. Mastri, M. Dionigi, and M. Mongiardo, "Wireless resonant-type power transfer links with relay elements: Harmonic balance design," in *Proc. 42nd Eur. Microw. Conf.*, Amsterdam, The Netherlands, Oct. 2012, pp. 225–228.
- [23] A. N. Laskovski and M. R. Yuce, "Class-E oscillators as wireless power transmitters for bio medical implants," in *Proc. 3rd Int. Symp. Appl. Sci. Biomed. Commun. Technol. (ISABEL)*, Rome, Italy, Nov. 2010, pp. 1–5.
- [24] A. Bassal, A. Shafiqurrahman, and A. Jarndal, "An Armstrong GaN-based oscillator for wireless power transfer applications," in *Proc. Int. Conf. Electr. Comput. Technol. Appl. (ICECTA)*, Ras Al Khaimah, United Arab Emirates, Nov. 2019, pp. 1–4.
- [25] R. L. O. Pinto, R. M. Duarte, F. R. Sousa, I. Müller, and V. J. Brusamarello, "Efficiency modeling of class-E power oscillators for wireless energy transfer," in *Proc. IEEE Int. Instrum. Meas. Technol. Conf. (I2MTC)*, Minneapolis, MN, USA, May 2013, pp. 271–275.
- [26] P. R. Troyk and G. A. DeMichele, "Inductively-coupled power and data link for neural prostheses using a class-E oscillator and FSK modulation," in *Proc. 25th Annu. Int. Conf. IEEE Eng. Med. Biol. Soc.*, Sep. 2003, pp. 3376–3379.
- [27] V. Ardila, F. Ramírez, and A. Suárez, "Nonlinear analysis of a high-power oscillator inductively coupled to an external resonator," *IEEE Microw. Wireless Compon. Lett.*, vol. 31, no. 6, pp. 737–740, Jun. 2021.
- [28] V. Ardila, F. Ramírez, and A. Suárez, "Nonlinear dynamics of an oscillator inductively coupled to an external resonator for power transfer and data transmission," *IEEE Trans. Microw. Theory Techn.*, vol. 70, no. 4, pp. 2418–2431, Apr. 2022.
- [29] V. Ardila, F. Ramírez, and A. Suárez, "Nonlinear analysis of an injection-locked oscillator coupled to an external resonator," *IEEE Microw. Wireless Compon. Lett.*, vol. 32, no. 6, pp. 740–743, Jun. 2022.
- [30] V. Ardila, F. Ramírez, and A. Suárez, "Analysis and design of injection-locked oscillators coupled to an external resonator," *IEEE Trans. Microw. Theory Techn.*, vol. 71, no. 10, pp. 4546–4561, Oct. 2023.
- [31] A. Gelb and W. Vander-Velde, *Multiple-Input Describing Functions and Nonlinear System Design*. New York, NY, USA: McGraw-Hill, 1968.
- [32] K. Kurokawa, "Some basic characteristics of broadband negative resistance oscillator circuits," *Bell Syst. Tech. J.*, vol. 48, no. 6, pp. 1937–1955, Jul. 1969.
- [33] V. Rizzoli and A. Lipparini, "General stability analysis of periodic steady-state regimes in nonlinear microwave circuits," *IEEE Trans. Microw. Theory Techn.*, vol. MTT-33, no. 1, pp. 30–37, Jan. 1985.
- [34] A. Suárez, *Analysis and Design of Autonomous Microwave Circuits*. Hoboken, NJ, USA: Wiley, 2009.
- [35] J. Guckenheimer and P. J. Holmes, *Nonlinear Oscillations, Dynamical Systems, and Bifurcations of Vector Fields*. New York, NY, USA: Springer, 1983.
- [36] A. Costanzo, M. Dionigi, F. Mastri, M. Mongiardo, J. A. Russer, and P. Russer, "Rigorous network modeling of magnetic-resonant wireless power transfer," *Wireless Power Transf.*, vol. 1, no. 1, pp. 27–34, Mar. 2014.
- [37] A. Ayachit, D. K. Saini, M. K. Kazimierzczuk, and T. Suetsugu, "Three-coil wireless power transfer system using class E² resonant DC–DC converter," in *Proc. IEEE Int. Telecommun. Energy Conf. (INTELEC)*, Oct. 2015, pp. 1–4.
- [38] J. de Cos, A. Suarez, and F. Ramirez, "Analysis of oscillation modes in free-running ring oscillators," *IEEE Trans. Microw. Theory Techn.*, vol. 60, no. 10, pp. 3137–3150, Oct. 2012.
- [39] H. Kawakami, "Bifurcation of periodic responses in forced dynamic nonlinear circuits: Computation of bifurcation values of the system parameters," *IEEE Trans. Circuits Syst.*, vol. CS-31, no. 3, pp. 248–260, Mar. 1984.
- [40] K. Ogata, *Modern Control Engineering*, 3rd ed. Upper Saddle River, NJ, USA: Prentice-Hall, 1997.
- [41] J. Jugo, A. Anakabe, and J. M. Collantes, "Control design in the harmonic domain for microwave and RF circuits," *IEE Proc. Control Theory Appl.*, vol. 150, no. 2, pp. 127–131, Mar. 2003.
- [42] J. M. Collantes, I. Lizarraga, A. Anakabe, and J. Jugo, "Stability verification of microwave circuits through floquet multiplier analysis," in *Proc. IEEE Asia–Pacific Conf. Circuits Syst.*, Dec. 2004, pp. 997–1000.
- [43] A. K. RamRakhyani and G. Lazzi, "On the design of efficient multi-coil telemetry system for biomedical implants," *IEEE Trans. Biomed. Circuits Syst.*, vol. 7, no. 1, pp. 11–23, Feb. 2013.
- [44] J.-Q. Zhu, Y.-L. Ban, Y. Zhang, Z. Yan, R.-M. Xu, and C. C. Mi, "Three-coil wireless charging system for metal-cover smartphone applications," *IEEE Trans. Power Electron.*, vol. 35, no. 5, pp. 4847–4858, May 2020.
- [45] J. Schaffner, "Simultaneous oscillations in oscillators," *Trans. IRE Prof. Group Circuit Theory*, vols. 1, no. 2, pp. 2–8, Jun. 1954.

- [46] I. Bruyland, "Simultaneous oscillations at two frequencies in RLC circuits," *Proc. IEEE*, vol. 56, no. 1, pp. 82–83, Jan. 1968.
- [47] F. Ramírez, S. Sancho, and A. Suárez, "Oscillation modes in multi-resonant oscillator circuits," *IEEE Trans. Microw. Theory Techn.*, vol. 64, no. 12, pp. 4660–4675, Dec. 2016.
- [48] R. M. Duarte and G. K. Felic, "Analysis of the coupling coefficient in inductive energy transfer systems," *Act. Passive Electron. Compon.*, vol. 2014, pp. 1–6, Jun. 2014.
- [49] J. J. Kim and J. Kim, "Modeling method of coil module for wireless power transfer system by two-port S-parameter measurement in frequency domain," in *Proc. IEEE Wireless Power Transf. Conf.*, May 2014, pp. 251–254.
- [50] A. Suárez and R. Quéré, *Stability Analysis of Nonlinear Microwave Circuits*. Norwood, MA, USA: Artech House, 2003.
- [51] M. Kiani, U.-M. Jow, and M. Ghovanloo, "Design and optimization of a 3-coil inductive link for efficient wireless power transmission," *IEEE Trans. Biomed. Circuits Syst.*, vol. 5, no. 6, pp. 579–591, Dec. 2011.
- [52] M. Machnoor, E. S. G. Rodríguez, P. Kosta, J. Stang, and G. Lazzi, "Analysis and design of a 3-coil wireless power transmission system for biomedical applications," *IEEE Trans. Antennas Propag.*, vol. 67, no. 8, pp. 5012–5024, Aug. 2019.
- [53] G. Monti, M. V. De Paolis, L. Corchia, A. Georgiadis, and L. Tarricone, "Efficiency optimization of a three-coil resonant energy link," *Wireless Power Transf.*, vol. 6, no. 2, pp. 126–137, Sep. 2019.
- [54] D.-W. Seo, "Comparative analysis of two- and three-coil WPT systems based on transmission efficiency," *IEEE Access*, vol. 7, pp. 151962–151970, 2019.



Víctor Ardila (Student Member, IEEE) was born in Bucaramanga, Santander, Colombia. He received the Engineer degree in mechatronics from the Autonomous University of Bucaramanga (UNAB), Santander, in 2013, and the Master of Engineering degree from the University of Málaga (UMA), Andalucía, Spain, in 2017. He is currently pursuing the Ph.D. degree in information technology and communications in mobile networks at the University of Cantabria (UC), Santander, Spain.

His research interests include the design and analysis of nonlinear circuits, and RF/microwave systems.



Franco Ramírez (Senior Member, IEEE) received the Licentiate degree in electronic systems engineering from the Military School of Engineering (EMI), La Paz, Bolivia, in 2000, and the Ph.D. degree in communications engineering from the University of Cantabria, Santander, Spain, in 2005.

From 1999 to 2000, he worked at Ericsson de Bolivia Telecomunicaciones, Santa Cruz de la Sierra, Bolivia, where he was involved in projects related to Global System for Mobile Communications (GSM) and Time-Division Multiple Access (TDMA) technologies. From 2009 to 2013, he was a Research Fellow of the "Ramón y Cajal" Program, funded by the Spanish Ministry of Science and Innovation, at the Communications Engineering Department, University of Cantabria, where he is currently an Associate Professor. His research interests include phase noise, stability, and the development of nonlinear techniques for the analysis and design of autonomous microwave circuits.



Almudena Suárez (Fellow, IEEE) was born in Santander, Spain. She received the Licentiate degree in electronic physics and the Ph.D. degree from the University of Cantabria, Santander, in 1987 and 1992, respectively, and the Ph.D. degree in electronics from the University of Limoges, Limoges, France, in 1993.

She has authored the book *Analysis and Design of Autonomous Microwave Circuits* (IEEE-Wiley, 2009) and coauthored the book *Stability Analysis of Nonlinear Microwave Circuits* (Artech House,

2003).

Prof. Suárez was a member of the Board of Directors of the European Microwave Association (EuMA) from 2012 to 2020. She is a member of the TPRCs of the IEEE International Microwave Symposium and European Microwave Week. She received the Research Award of the Social Council of the University of Cantabria in 2021. She was an IEEE Distinguished Microwave Lecturer from 2006 to 2008. She was the Coordinator of the Communications and Electronic Technology Area for the Spanish National Evaluation and Foresight Agency (ANEP) from 2009 to 2013. She has been the Publication Officer of EuMA since 2021. She was the Chair of the 2014 and 2015 editions of IEEE Topical Conference on RF/Microwave Power Amplifiers (PAWR), in Newport Beach and San Diego. She was the General TPC Chair of EuMW 2018. She was the Chair of the IEEE Subcommittee for the Best Paper Award in *IEEE Microwave Magazine* from 2017 to 2022. She was the Editor-in-Chief of the *International Journal of Microwave and Wireless Technologies* of Cambridge University Press journals from 2013 to 2018 and an Associate Editor of *IEEE Microwave Magazine* from 2014 to 2022. Since October 2022, she has been the Editor-in-Chief of IEEE TRANSACTIONS ON MICROWAVE THEORY AND TECHNIQUES.